ACS Catalysis

Research Article

pubs.acs.org/acscatalysis

Elucidating Structure–Property Relationships in the Design of Metal Nanoparticle Catalysts for the Activation of Molecular Oxygen

Christopher S. Hinde,[†,‡] Davide Ansovini,[†] Peter P. Wells,[#,Δ] Gillian Collins,[∥,⊥] Sivan Van Aswegen,[†] Justin D. Holmes,[∥,⊥] T. S. Andy Hor,[‡,§] and Robert Raja*[,†]

[†]School of Chemistry, University of Southampton, Southampton SO17 1BJ, U.K.,

[‡]Institute of Materials Research and Engineering (IMRE), A*STAR, 3 Research Link, Singapore 117602

[#]UK Catalysis Hub, Research Complex at Harwell, Harwell, Oxon OX11 0FA, U.K.

[Δ]Kathleen Lonsdale Building, Department of Chemistry, University College London, Gordon Street, London WC1H 0AJ, U.K.

[∥]Department of Chemistry and Tyndall National Institute, University College Cork, Cork, Ireland

[⊥]AMBER@CRANN, Trinity College Dublin, Dublin 2, Ireland

[§]Department of Chemistry, National University of Singapore, 3 Science Drive 3, Singapore 117543

Supporting Information

ABSTRACT: A novel synthetic strategy for the design of metal nanoparticles by extrusion of anionic chloride precursors from a porous copper chlorophosphate framework has been devised for the sustainable aerobic oxidation of vanillyl alcohol (4-hydroxy-3-methoxybenzyl alcohol) to vanillin (4-hydroxy-3-methoxybenzaldehyde) using a one-step, base-free method. The precise nature of the Au, Pt, and Pd species has been elucidated for the as-synthesized and thermally activated analogues, which exhibit fascinating catalytic properties when subjected to diverse activation environments. By employing a combination of structural and spectroscopic characterization tools, it has been shown that analogous heat treatments have differing effects on extrusion of a particular metal species. The most active catalysts in this series of materials were the extruded Pt nanoparticles that were generated by reduction in H_2, which exhibit enhanced catalytic behavior, when compared to its Au or Pd counterparts, for industrially significant, aerobic oxidation reactions.

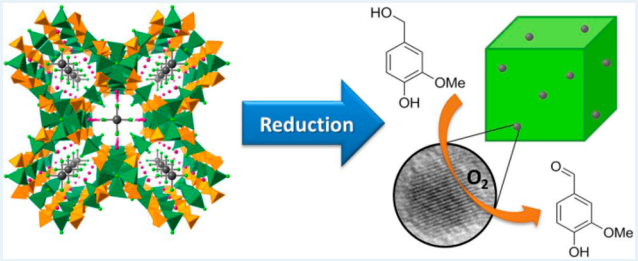

KEYWORDS: *nanoparticle, catalysis, vanillyl alcohol, structure–property correlations, aerobic oxidation, vanillin, EXAFS*

INTRODUCTION

Design of versatile metal nanoparticle (NP) catalysts has been a progressive area of research within the field of heterogeneous catalysis in recent years, due to their significant potential in a variety of chemical transformations, including industrially desirable selective aerobic oxidations. Monometallic (Au, Pt, Pd) and bimetallic NPs have been successfully employed in the selective oxidation of alcohols,[1] including glycerol,[2] cinnamyl alcohol,[3] crotyl alcohol[4,5] and benzyl alcohol,[6,7] to name but a few. Prodigious design of bimetallic equivalents has recently demonstrated their propensity for C–H activation, particularly in the oxidation of aromatics.[8,9] In addition to bulk chemical applications, heterogenized Pd NPs have also found a niche for cross-coupling reactions, alongside their ubiquitous homogeneous counterparts.[10] The key to engineering catalytically active NPs reproducibly appears to be contingent on the development of robust design strategies that can control the size and shape of the particles at the nanoscale, which still proves to be a challenge.[11]

A variety of preparation methods for generating NPs on solid supports have been previously studied with specific focus on control of the nanoparticle size and shape.[11−14] These include wet impregnation,[15] deposition–precipitation[16] and sol–immobilization techniques,[17,18] with the latter showing a greater propensity for the generation of smaller particle sizes, but often resulting in polymer-capped particulates and hence a reduction in accessible surface area. More importantly, these research efforts have clearly illustrated that changes in size, ranging from average diameters of less than 1 nm up to 10 nm, can have a substantial effect on catalytic activity,[11,12,19] with smaller particle sizes affording superior conversion rates in most cases. In fact, studies involving cluster-based nanoparticle catalysts even highlighted the integral importance of site-isolation as well as particle size in enhancing efficiency of catalytic oxidations and hydrogenations.[20−25] The nature of support materials has ranged from metal oxides[26] and carbonaceous materials,[27] to microporous alternatives such as zeolites[28,29] or metal–organic frameworks (MOFs),[30,31] and

Received: March 6, 2015
Revised: April 10, 2015
Published: May 14, 2015

DOI: 10.1021/acscatal.5b00481
ACS Catal. 2015, 5, 3807−3816

mesoporous silica-derived hosts[32] such as MCM-41 or SBA-15. Nanoporous materials have been extensively explored for their intrinsic catalytic properties;[33] however, isolated single-sites in the form of doped frameworks[34−36] or supported nanoparticles have proved to be superior. The latter have afforded a better understanding of the nature of the active site at the molecular level, which has resulted in the development of heterogenized NP catalysts with unprecedented activity.[21−24]

We have recently demonstrated a novel strategy for generating uniform sized, small NPs (ca. 5 nm) by extrusion of MCl_x precursor complex anions (M = Au, Pt or Pd) from a crystalline microporous copper chlorophosphate framework (Figure 1).[7] The framework is of Cu-2 topology[37] and has

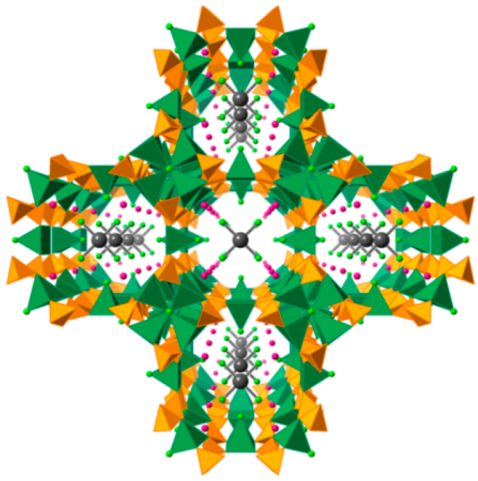

Figure 1. Representative crystal structure of the $[PtCl_4]^{2-}$ supported $Rb_9Cu_6(P_2O_7)_4Cl_2$ framework (Pt − gray spheres, Cl − green spheres, Rb − pink spheres, Cu − green polyhedra, P − orange polyhedra, oxygen omitted for clarity).

flexible anion-exchange properties.[38] In this article, we rationalize and demonstrate the efficacy of our design strategy for the in situ generation of nanoparticles within a microporous host architecture, wherein the porous framework can be employed synergistically as an active species, and not just as a heterogeneous support, thereby affording exciting prospects for bifunctional catalysis. We have meticulously probed the nature of the active site using a combination of X-ray absorption spectroscopy (XAS), X-ray photoelectron spectroscopy (XPS), and transmission electron microscopy (TEM), for affording structure−property correlations, which highlight the efficacy of catalyst activation protocols on metal (NP) extrusion and ensuing catalytic activity. These findings further confirmed the structural and compositional integrity of the active sites, that subsequently led to the design and creation of well-defined and isolated heterogeneous NP catalysts for the aerobic oxidation of vanillyl alcohol (Scheme 1), using a one-step, base-free method.

The production of vanillin is significant in the fine chemicals industry, as its primary use in vanilla flavorings and fragrances make it the single-most highly produced additive in this field.[39] Demand for food-grade vanillin has led to a production rate of approximately 12 000 tons per annum, of which natural vanilla extracts contribute only 20 tons.[40] It is also used in other industries, including as an intermediate toward pharmaceuticals such as L-3,4-dihydroxy-phenylalanine (L-DOPA), a key therapeutic agent used to combat Parkinson's disease. Current

Scheme 1. Aerobic Oxidation of Vanillyl Alcohol to Vanillin and Vanillic Acid

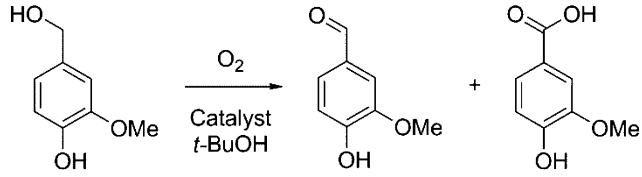

synthetic methods employ one of three routes: (i) an established method that utilizes the degradation of lignins, which is a solvent intensive process involving multiple extraction and distillation steps;[40] (ii) a cheaper synthetic pathway from guaiacol (Schemes 2 and 3), but which involves

Scheme 2. Industrial Synthetic Procedure for Synthesis of Vanillin (2) from Guaiacol (1) via Glyoxylic Acid[40]

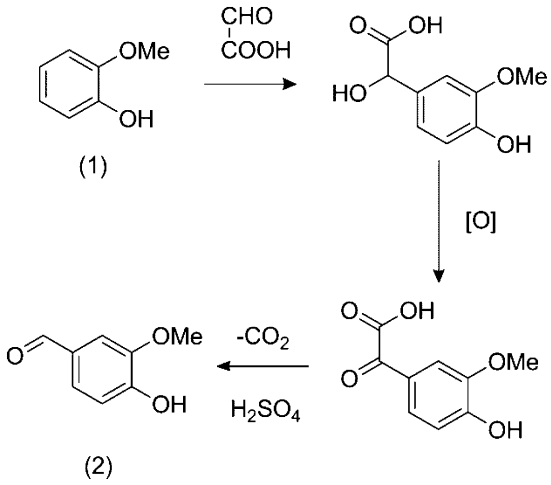

Scheme 3. Industrial Synthetic Procedure for Synthesis of Vanillin from Guaiacol via Formaldehyde (See SI)[41]

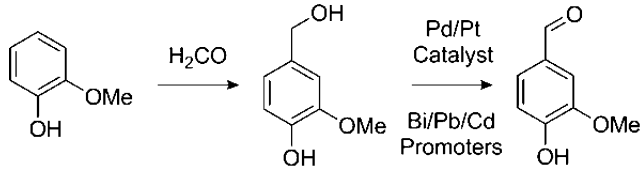

the use of mineral acids and heavy-metal promoters such as Pb, Bi, and/or Cd;[40,41] or (iii) a biosynthetic pathway, which involves high production costs.[42,43] Schemes 2 and 3 represent the processes mostly employed in industry today, both of which are composed of the same principles: first, a condensation reaction with either glyoxylic acid (Scheme 2) or formaldehyde (Scheme 3), followed by an oxidation step and subsequent decarboxylation. The route via glyoxylic acid requires the decarboxylation step to form the desired product, vanillin. The formaldehyde route, however, produces small quantities of vanillin (16%) after the oxidation step, with the decarboxylation converting some of the overoxidation products back to vanillin, in order to obtain an overall yield of 61%[41] (detailed scheme in Figure S1.1). It is to be noted that both methods involve multistep processes to achieve these yields.

The catalytic activation of molecular oxygen is therefore of significant interest and poses a substantial challenge for the fine-chemicals industry; this is especially true in selective

DOI: 10.1021/acscatal.5b00481
ACS Catal. 2015, 5, 3807−3816

oxidations, with the selective oxidation of vanillyl alcohol to vanillin being a compelling example. Due to the benign nature of molecular oxygen, its utilization as a potential oxidant[44] can help mitigate the use of hazardous reagents, which lead to the generation of greenhouse gases and wasteful byproducts (Schemes 2 and 3).[45] From an academic and industrial standpoint, the concomitant use of a heterogeneous catalyst with molecular oxygen affords many advantages from a socio-economic and environmental perspective, as it offers a viable alternative to homogeneous processes that currently generate stoichiometric quantities of toxic inorganic waste,[46] thereby impeding the atom-efficient synthesis of fine-chemicals and pharmaceuticals.

EXPERIMENTAL SECTION

Chemicals for synthesis and catalytic tests were purchased from Sigma-Aldrich, Fisher Scientific, or Acros Organics and used without further purification.

Material Synthesis. Copper(II) fluoride (0.1168 g, 1.150 mmol), 85 wt % orthophosphoric acid (0.2 mL, 2.922 mmol), 50 wt % RbOH (0.24 mL, 2.037 mmol), RbCl (0.28 g; 2.316 mmol) and a source of MCl_x; $HAuCl_4$ (0.0489 g, 0.144 mmol), K_2PtCl_4 (0.0515 g, 0.124 mmol) or K_2PdCl_4 (0.0405 g, 0.124 mmol) were mixed in the Teflon liner of a custom-made 23 mL hydrothermal vessel. The vessel was sealed and heated to 448 K for 2 days.

Products formed as brilliant green cuboid crystals for both the Au and Pt material and as light brown crystals for the Pd material. Materials were further activated either by calcination (air, 773 K, 2 h) or reduction (5% H_2/N_2, 473 K, 2 h) to generate the active nanoparticle catalysts. After calcination, the Au and Pd materials appeared unchanged in color, but the Pt catalyst changed to a darker khaki-green. After reduction, the Au material appeared unchanged, the Pt material appeared a more dark green color than the calcined equivalent, and the Pd material appeared black in color.

X-ray Photoelectron Spectroscopy. XPS analysis was performed using a Thermo Scientific Theta Probe instrument equipped with monochromated Al Kα source in NEXUS, University of Newcastle. A flood gun was used for charge compensation. A pass energy of 200 eV and a step size of 1.0 eV was employed for all survey spectra while a pass energy of 40 eV and a step size of 0.1 eV was used for high-resolution spectra of the elements of interest. All XPS spectra were calibrated against the carbon and/or oxygen 1s peaks, and high-resolution spectra were fitted with Shirley backgrounds before peak analysis using the CasaXPS software.[47]

X-ray Absorption Spectroscopy. Pd, Pt, and Au XAFS studies were carried out on the B18 beamline at the Diamond Light Source, Didcot, U.K. Measurements were performed using a quick extended X-ray absorption fine structure (QEXAFS) setup with a fast-scanning Si (111) or Si (311) double crystal monochromator. The normal time resolution of the spectra reported herein was 1 min/spectrum (k_{max} = 16); on average, six scans were acquired to improve the signal-to-noise level of the data. All samples were diluted with cellulose and pressed into pellets to optimize the effective edge-step of the XAFS data and measured in transmission mode using ion chamber detectors. All transmission XAFS spectra were acquired concurrently with the appropriate reference foil placed between I_t and I_{ref}. XAS data processing and EXAFS analysis were performed using IFEFFIT[48] with the Horae package[49] (Athena and Artemis). The amplitude reduction factor, s_o^2, was derived from EXAFS data analysis of known compounds and used as a fixed input parameter.

Transmission Electron Microscopy. TEM analysis was performed on a Jeol 2100 Electron Microscope at an operating voltage of 200 kV. The catalyst framework was prone to damage by the electron beam. Therefore, to minimize sample degradation, the TEM images were collected quickly to mitigate the above.

Catalysis. Catalytic reactions were carried out in a 75 mL PTFE lined, stainless-steel, high-pressure batch reactor. The reactor was charged with vanillyl alcohol (1 g), diethylene glycol dimethyl ether (0.85 g) as an internal standard, *tert*-butanol (30 mL) as a solvent and catalyst (50 mg). The reactor was pressurized with ≈20 bar of dry air, stirred, and heated for the required amount of time. Small aliquots of the reaction mixture were taken carefully periodically for GC analysis. Samples were analyzed by GC (PerkinElmer, Clarus 480) using an Elite-5 column equipped with a flame ionization detector (FID). Products were identified against authenticated standards and quantified by calibration to obtain response factors (R_F) against the known internal standard.

RESULTS AND DISCUSSION

Figure 2 shows the non-phase-corrected Fourier transform (both magnitude and imaginary component) of the k^3 weighted EXAFS data for the reduced Pd, Pt, and Au catalyst materials, with the fitting parameters generated detailed in Table 1. The EXAFS data of the reduced Pt sample is consistent with that expected for Pt nanoparticles. The long-range structure in the

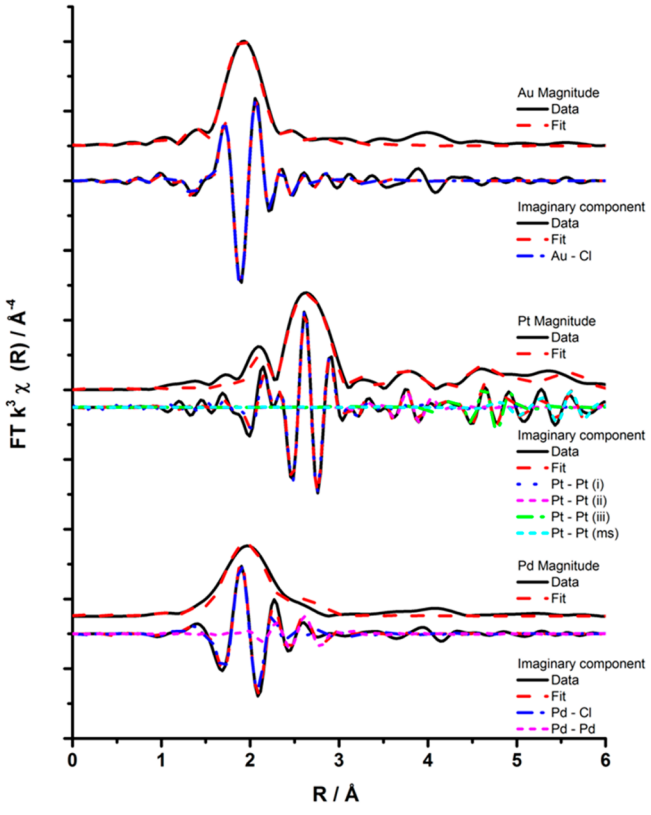

Figure 2. Magnitude and imaginary component of the k^3 weighted Fourier transform for the EXAFS data of the reduced Pd (bottom), Pt (middle), and Au (top) samples. Associated scattering paths are included for the imaginary component.

DOI: 10.1021/acscatal.5b00481
ACS Catal. 2015, 5, 3807−3816

Table 1. EXAFS Fitting Parameters for the Reduced Pd, Pt and Au Samples[a]

sample	abs sc	N	R/Å	$2\sigma^2$/Å^2	E_f/eV	R_{factor}
reduced Au sample	Au−Cl	3.7 (2)	2.29 (1)	0.002 (1)	10 (1)	0.005
reduced Pd sample	Pd−Cl	3.3 (3)	2.35 (1)	0.003 (1)	10 (2)	0.004
	Pd−Pd	1.3 (5)	2.77 (2)	0.004 (2)		
reduced Pt sample	Pt − Pt	8.4 (5)	2.76 (1)	0.005 (1)	7 (2)	0.007
	Pt−Pt	3 (1)	3.91 (2)	0.005 (1)		
	Pt−Pt	10 (3)	4.79 (2)	0.007 (1)		
	Pt−Pt (ms)	13 (3)	5.65 (2)	0.011 (2)		

[a]Fitting parameters: (Au sample) S_0^2 = 0.75 as deduced by $KAuCl_4$ standard; Fit range 3.5 < k < 12.5, 1.1 < R < 3; no. of independent points = 10; (Pd sample) S_0^2 = 0.82 as deduced by $PdCl_2$ standard; Fit range 3 < k < 11.5, 1 < R < 3; no. of independent points = 11; (Pt sample) S_0^2 = 0.91 as deduced by Pt foil standard; Fit range 3.5 < k < 14, 1 < R < 6; no. of independent points = 32.

radial distribution function is indicative of metallic particles, and EXAFS data can be modeled by including the contribution from the nearest three Pt−Pt distances and a multiple scattering Pt−Pt path from the primary Pt coordination shell. The coordination number for the primary Pt coordination shell is smaller (8.4) than that expected for a bulk Pt structure (12), indicating the nanoparticulate nature of the Pt sample (Table 1). In addition, by using an analogous EXAFS analysis, which was previously employed[50] for the calculation of particle sizes from CNs of the first shell of a face-cented cubic (fcc) system, we have estimated that our Pt NPs possess average diameters of 1.4 nm. The EXAFS data of the reduced Pd sample is similar to the initial Pd precursor used for the preparation of the materials, with the largest contribution in the Fourier transform resulting from the primary Pd−Cl coordination shell. However, the EXAFS data also suggests the presence of Pd nanoparticles as indicated by a second feature in the imaginary part of the Fourier transform, which is consistent with a Pd−Pd scattering distance. The weak Pd−Pd contribution is evidence that only a small fraction of Pd sites are present as metallic species, with the majority of Pd sites consistent with the initial catalyst precursor. The radial distribution plot for the reduced Au sample is dominated by one component, which can be assigned to an Au−Cl scattering path. There is a good degree of correlation between the EXAFS data of the reduced Au sample and the KAuCl4 precursor, indicating that the significant component in this reduced sample is the $[AuCl_4]^-$ anion. Although there is no observable metallic contribution from the EXAFS data, some NP formation is clearly observed (see XPS and TEM data) and is present at least in a minor fraction. It is also noteworthy that the EXAFS data for the calcined material shows evidence of metallic Au (Figure S2.1); however, the similarity with the Au reference foil indicates mostly larger nanoparticles with more bulk properties.

XAS data was also obtained for the calcined Pt and Pd materials (Figures S2.2, S2.3); however for the most part, due to XAS being a bulk analysis technique, the data for the Pt and Pd matched quite closely with the standards collected for the respective precursor chloride materials. This highlights the fact that only a small quantity of the chlorometallate anions have been extruded, in comparison with the reduced samples, to form nanoparticles. It is well-known that $[AuCl_4]^-$ can be reduced thermally in the presence of any gas,[51] which explains the presence of metallic species for the calcined Au material. However, the Pt and Pd materials require much more specific reducing conditions, as outlined in the Experimental Section, for the generation of nanoparticles.

High-resolution XPS data were also acquired in order to further probe the nature of the metallic species, and to contrast these findings with the XAS studies. As can be seen in the XPS spectra for the Au samples (Figure 3), a signal for Au(0) is

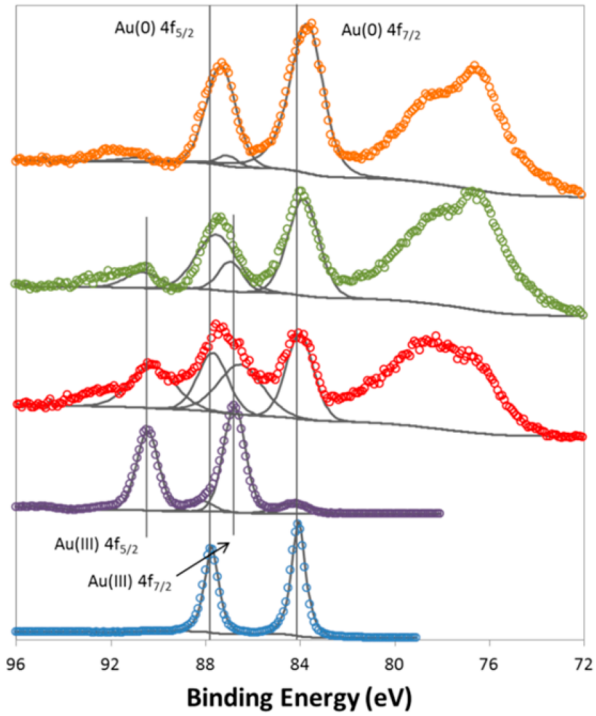

Figure 3. XPS spectra of metallic Au (blue circles) and $KAuCl_4$ (purple circles) standards, and as-synthesized (red circles), calcined (green circles) and reduced (orange circles) Au materials. (Black lines indicate background and component peaks.)

present not only in the reduced sample but also in the calcined and as-synthesized materials. It is highly likely that these are generated from small amounts of larger crystalline gold impurities in the synthesis procedure, before the actual formation of the crystalline framework. This is apparent from the observation that the Au(0) $4f_{7/2}$ signal has a binding energy that is typical of bulk gold at 84.1 eV. It was further noted in the calcined sample that the presence of the Au(0) signal increases relative to that of the Au(III) $4f_{7/2}$ signal at 86.8 eV, but a slight shift to lower binding energy for the Au(0) $4f_{7/2}$ to 83.9 eV was observed. Furthermore, for the reduced sample, almost complete conversion of Au(III) to Au(0) was observed, with a greater shift in the Au(0) $4f_{7/2}$ peak to a lower binding energy of 83.6 eV. This shift to a lower binding energy for the Au(0) peaks has been observed, as a notable characteristic, for the formation of nanoparticulate gold.[52,53] Miller et al.[52] attribute

DOI: 10.1021/acscatal.5b00481
ACS Catal. 2015, 5, 3807−3816

this phenomenon to a change in the local electronic structure close to the Fermi level of the small nanoparticles, in comparison with bulk gold.

In stark contrast to XAS, XPS is a surface sensitive technique, and thus, it is interesting to note the presence of metallic Au NPs in the XPS, even though a larger proportion of the Au present was shown to manifest as $[AuCl_4]^-$ from the EXAFS measurements (Figure 2). Given that the sampling volume of XPS analysis has a depth less than 10 nm and that the crystallite sizes are approximately 20 μm,[7] these results indicate that our materials are composed of isolated fractions of surface NPs and hence represent distinct, discrete regions of Au species.

The large peak adjacent to the Au 4f peaks at lower binding energy (76−78 eV) in the XPS spectra (Figure 3) is associated with a Cu 3p signal originating from the framework. Although this is clearly resolved from the Au peaks in Figure 3, there is some overlap with the Pt 4f peaks, as can be seen in Figure 4.

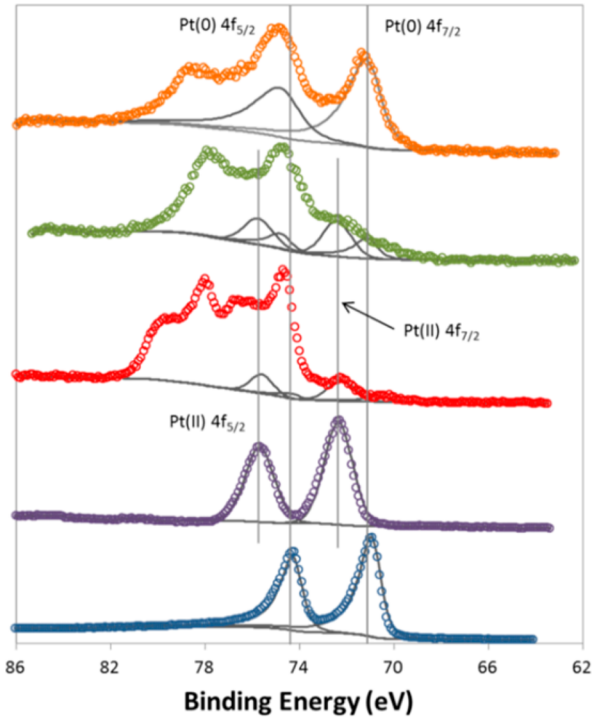

Figure 4. XPS spectra of metallic Pt standard (blue circles) and K_2PtCl_4 standard (purple circles), and as-synthesized (red circles), calcined (green circles), and reduced (orange circles) Pt materials. (Black lines indicate background and component peaks.)

For the sake of clarity, only peaks from the Pt have been displayed in Figure 4 (see Figure S3.1 for an exemplar fitting with Cu 3p assignments). From the Pt XPS data, we can observe a similar trend to the Au materials; namely, calcination of the as-synthesized Pt sample results in the generation of a small quantities of Pt(0) that is apparent at 71.2 eV (compared with Pt(II) at 72.4 eV). However, the most striking observation was noted for the reduced sample (Figure 4), where the almost complete reduction of the Pt(II) is apparent, with only peaks associated with the metallic Pt(0) dominating the spectra. These results, juxtaposed with observations from the EXAFS data (Figure 2 and Table 1), further corroborate our findings relating to the complete reduction of the $[PtCl_4]^{2-}$ species to metallic NPs.

XPS data from the Pd 3d region of the spectra (Figure 5) clearly show a transition from a mixture of Pd(IV) and Pd(II)

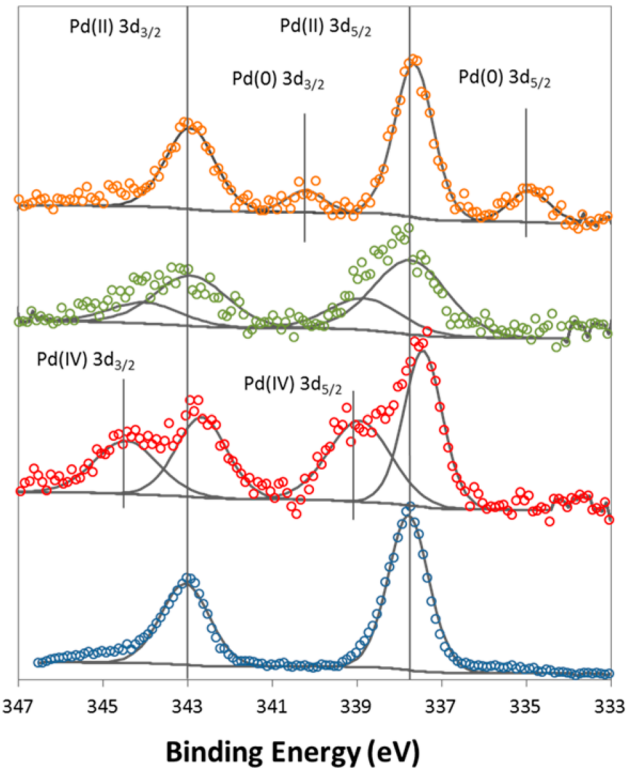

Figure 5. XPS spectra of K_2PdCl_4 standard (blue circles) and as-synthesized (red circles), calcined (green circles), and reduced (orange circles) Pd materials. (Black lines indicate background and component peaks.)

species in the as-synthesized material (binding energies of 338.9 and 337.6 eV respectively), to predominantly Pd(II) in the calcined analogues, with some indications for the presence of Pd(0) (335.0 eV), in the reduced samples. A clear contribution of Pd(IV) was noted in some of our samples. A related study[54] dealing with the location of supported Pt(II) species noted that, in close proximity, a mixed valence Pt(II)−Pt(IV) bonded dimer was formed, the presence of which was further substantiated by DFT calculations. It is highly plausible that a similar mechanism is operating in our systems, where mixed-valence dimers are formed as precursors to cluster formation, prior to nucleation and eventual nanoparticle growth. This, in conjunction with the EXAFS data, clearly shows that, although the reduction process seems to be much better for extruding nanoparticles than calcination, the presence of metallic Pd(0) is still minor, in comparison with Pd(II) species. We can also conclude that the EXAFS data provide no evidence of any significant PdO_x phase, with the major contribution in the Fourier transform associated with the characteristic scattering of Pd−Cl (Figure 2). EXAFS data was also acquired for a PdO standard (Figure S2.4), which illustrates two distinct shells (Pd−O and Pd−Pd scattering paths) in the Fourier transform, that are not present in the data obtained for our Pd materials. This supports our assertion that Pd oxide particles are not produced during the synthesis procedure and that the Pd(II) species are predominantly associated with the abundant chlorometallate precursor anions, as in the as-synthesized materials.

DOI: 10.1021/acscatal.5b00481
ACS Catal. 2015, 5, 3807−3816

It is interesting to note that, although identical conditions were used for thermally activating the analogous metalchloride supported frameworks, the Pt material appears much more readily amenable and susceptible to nanoparticle formation by extrusion, than the Au or Pd. This could be attributed to the differing strength of interactions between the discrete chlorometallate anions within the framework channels and the framework matrix. Further work is currently in progress to study the calcination and reduction protocols in greater detail using in situ X-ray absorption spectroscopy coupled with high-resolution electron microscopy (using high-angle annular dark-field imaging and tomography).

TEM analysis of the reduced catalysts are shown in Figure 6, which reveal that the Au, Pt, and Pd catalyst frameworks are

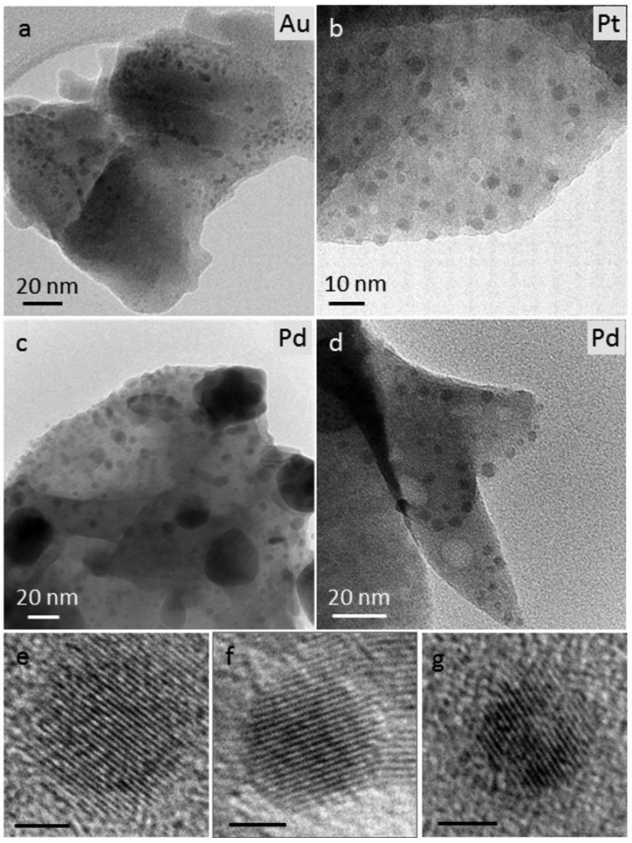

Figure 6. TEM images of reduced (a) Au, (b) Pt and (c)−(d) Pd catalysts, with magnified images of individual Au (e), Pt (f), and Pd (g) nanoparticles (scale bars in (e)−(g) are 2 nm).

composed of coexisting crystalline and amorphous phases. The presence of crystalline embedded nanoparticles, with typical diameters of 2−6 nm, can be seen in Figure 6b. High-resolution TEM analysis, shown in Figure 6e,f, display particles with measured fringe spacings of 0.2 and 0.23 nm, which can be attributed to Au(200) and Pt(111), respectively.[55] The mean diameter of the Pt NPs estimated from TEM is 2.6 nm (std dev = 0.7) (Figure S4.1), which is slightly higher than that estimated by analysis of the EXAFS data, but certainly in agreement with overall particle sizes, which are less than 3 nm across the bulk of the material. The sizes are smaller than that previously reported for NPs extruded by calcination in air at 500 °C,[7] with both the lower temperature and reducing conditions favoring smaller NP formation. It should be noted, however, that a thorough high-resolution TEM study was hindered by the beam sensitivity of the catalysts. The morphology of the reduced Pd catalysts shows some differences compared to the Au and Pt catalysts, with the presence of larger particles (20−50 nm) embedded in an amorphous matrix, as shown in Figure 6c. Due to sensitivity (dynamic changes in crystal orientation) of the sample under the electron beam,[56] the atomic resolution crystallinity of these particles could not be probed in greater detail. However, there is evidence of some Pd nanoparticle formation, as seen in Figure 6g, displaying lattice fringes of 0.22 nm, characteristic of Pd(111).[55] The Pd nanoparticles are innately located at the edges of the composite material.

All three catalysts (calcined and reduced under identical conditions, as outlined in the Experimental Section) were probed for their catalytic potential, with a view to establishing some initial trends that could be rationalized not only on the basis of the shape and size of the nanoparticles but also, more importantly, on their propensity to readily extrude from their crystalline microporous framework. The aerobic oxidation of vanillyl alcohol to vanillin, an intermediate step in the industrial process to form vanillin from guaiacol (Schemes 2 and 3), was used as a model probe reaction, given its importance from a technological perspective. Interestingly, as reported in Figure 7a, all three reduced catalysts displayed high activities for this aerobic oxidation, with the reduced Pt analogue affording close to 100% conversion and selectivities for vanillin in excess of 80%, for this one-step process that we have devised (in contrast with the multistep processes that are currently employed). Given the challenging aspects of this aerobic oxidation, turnover numbers (TONs) obtained with the Au and Pd catalysts were modest. However, the performance of the corresponding Pt analogue far exceeded that of its Au and Pd counterparts, with the reduced Pt catalyst, to the best of our knowledge, yielding unprecedented turnover values for this aerobic oxidation at moderate reaction conditions (Figure 8). This clearly highlights the superior role of the Pt NP catalyst, in this series of materials, for aerobic oxidation reactions. From the XPS and EXAFS data, the high activity of the Pt material can be attributed to the complete extrusion of the $[PtCl_4]^{2-}$ precursor, to yield stabilized discrete nanoparticles that are amenable for catalysis, in stark contrast with the Au and Pd materials (Figures 2 and 4).

The catalytic oxidation is composed of three main steps, namely: (i) the adsorption of the alcohol on the surface with the formation of a metal-alcoholate species; (ii) the β-hydride elimination that results in the formation of the metal-hydride intermediate and the carbonyl compound, which subsequently desorbs; and (iii) the oxidation of the metal hydride intermediate with concomitant formation of water and subsequent regeneration of the metallic active site, which is now available for further catalytic turnover.[1,19,57] The resulting product selectivity from the catalytic reaction is outlined in Figure 7b, from where it is possible to distinguish different trends, in relation to the specific examined catalyst. The reduced Pt catalyst affords the highest vanillin selectivity (>80%), which is relatively consistent, except for the formation of a small quantities of vanillic acid after prolonged contact times. The vanillin selectivity for the reduced Pd material increases steadily over time, but the corresponding reduced Au catalyst displays a distinctly different behavior compared to the others, with the selectivity toward vanillin decreasing monotonically with reaction time. The formation of the byproduct 4-hydroxy-3-methoxybenzyl *tert*-butyl ether was

DOI: 10.1021/acscatal.5b00481
ACS Catal. 2015, 5, 3807−3816

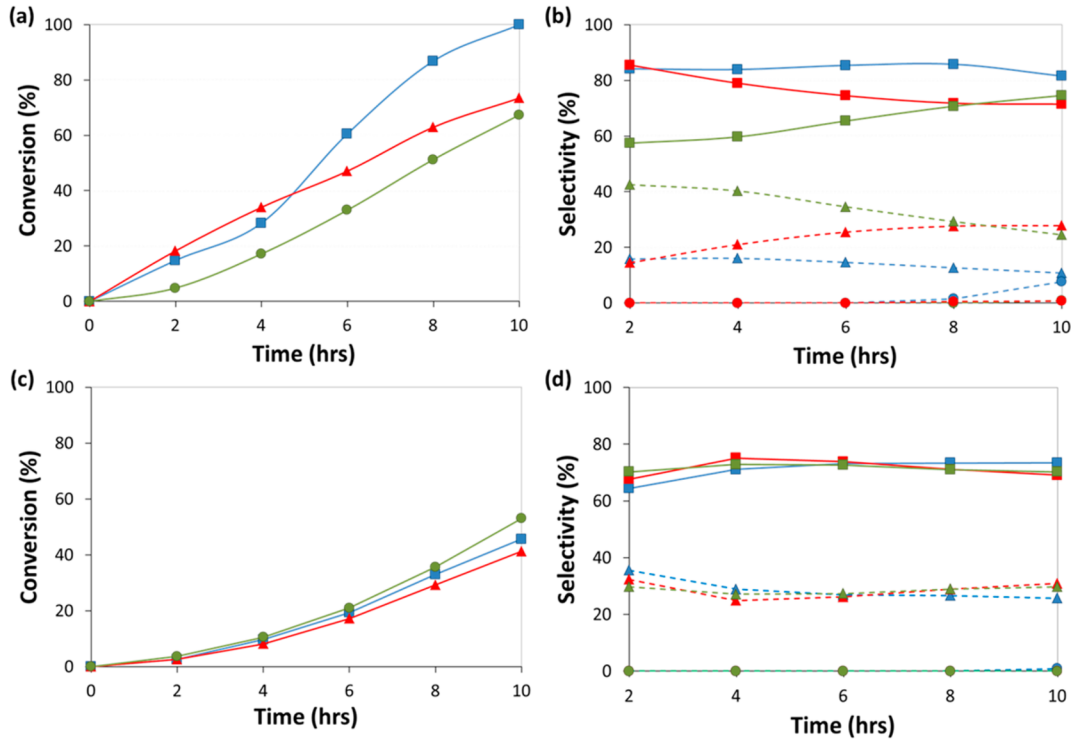

Figure 7. Kinetic plots outlining the catalytic activity for the Au (red triangles), Pt (blue squares), and Pd (green circles) reduced (a) and calcined catalysts (c). Corresponding selectivity profiles of Au (red), Pt (blue), and Pd (green) reduced (b) and calcined catalysts (d) toward vanillin (squares), 4-hydroxy-3-methoxybenzyl *tert*-butyl ether (triangles), and vanillic acid (circles). Reaction conditions: vanillyl alcohol (1 g), *tert*-butanol (30 mL), diglyme (0.85 g), catalyst (50 mg), T = 170 °C, P_{air} (20 °C) = 20 bar.

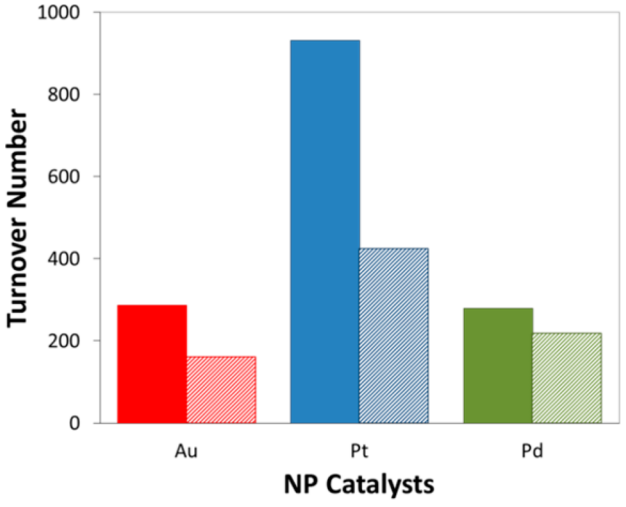

Figure 8. Comparison of catalytic turnover for Au (red), Pt (blue), and Pd (green) reduced (solid) and calcined (patterned) catalysts. See Figure 7 for reaction conditions.

confirmed using gas chromatography-mass spectrometry (GC-MS) analysis, and it was noted that the selectivity for this particular product increases over time for the Au catalyst. The origin of the 4-hydroxy-3-methoxybenzyl *tert*-butyl ether can be readily rationalized on the basis of the generation of a hydride species,[57,58] that induces local acidity in the nanoparticle, thus facilitating the etherification between the stabilized vanillyl alcoholate and the adsorbed *tert*-butanol solvent molecules (Scheme 4). It is well-known that *p*-hydroxybenzylic alcohols can undergo an etherification reaction in presence of another alcohol under acidic or harsh oxidative conditions.[59] Although

Scheme 4. Etherification of Vanillin with *t*-Butanol To Form Byproduct

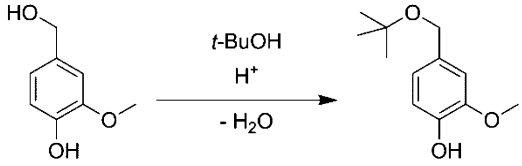

this is known for Au systems,[57,58] it is highly likely that similar mechanisms are also facilitating the formation of this product (4-hydroxy-3-methoxybenzyl *tert*-butyl ether) for the Pt and Pd catalysts, though with varying kinetics of hydride formation, which accounts for the different selectivities observed with these catalysts, when compared to the Au analogue. Detailed kinetic analyses are currently ongoing, and these will be published separately.

In order to investigate the effect of temperature on the catalytic activity of the materials, analogous reactions were performed at 150 °C. In line with our expectations, the lower temperatures afforded reduced activity but more importantly resulted in a comparatively higher selectivity toward the ether product (Table 2). It was indeed revealing that lower reaction temperatures facilitated the stabilization of the metal−alcoholate complex, thereby inducing a higher propensity for etherification. In addition to this, the adsorption stability of the formed aldehyde was higher at lower reaction temperatures, leading to longer induction periods in the catalysis. However, the reduced Pt catalyst again affords the highest selectivity toward the target product (vanillin), when compared to the Au and Pd analogues, despite its activity being drastically inferior when compared to the catalytic tests at 170 °C (Figure 7a).

DOI: 10.1021/acscatal.5b00481
ACS Catal. 2015, 5, 3807−3816

Table 2. Kinetic Data for the Aerobic Oxidation of Vanillyl Alcohol at 150 °C[a]

			selectivity (%)			
metal	time (h)	conv (%)	vanillin	ether[b]	acid[c]	TON[d]
Pt	8	14.35	74.15	25.85	0	133
	10	32.25	76.00	24.00	0	298
Au	8	35.79	54.06	45.94	0	140
	10	42.03	55.61	44.39	0	164
Pd	8	24.11	51.41	48.59	0	99
	10	32.38	52.83	47.17	0	133

[a]For reaction conditions (excluding temperature), see Figure 7. [b]4-hydroxy-3-methoxybenzyl *tert*-butyl ether. [c]Vanillic acid. [d]TON based on conversion of vanillyl alcohol.

Thus, in order to maximize both conversions and selectivities to the desirable vanillin, higher reaction temperatures must be employed in this particular system.

Analogous reactions were also carried out with the calcined catalysts, in order to make reactivity/selectivity comparisons with those of the reduced counterparts described in Figure 7a,b. As can be seen from Figure 7c,d, there is very little difference in the reactivity and selectivity profiles for all three catalysts. It is however significant that the latter (calcined catalysts) are markedly inferior in catalytic performance when compared with their reduced analogues, which further indicates the superior performance of the reduced materials, and in particular the Pt catalyst. The catalytic performance of these materials can indeed be rationalized from the XPS data (Figure 4), which reveals an enhancement in the *metallic* character of the reduced Pt catalyst, which are clearly the desired active sites for this aerobic oxidation reaction. Consistent with the above, the pronounced increase in activity for the reduced Au catalyst, when compared with its calcined analogue, can also be corroborated from the detection of higher quantities of nanoparticulate gold, as confirmed from the shift in the binding energies in the XPS spectra (Figure 3). It was therefore unsurprising to note that only a marginal difference was observed in the catalytic activity of the reduced Pd catalyst, when compared with its calcined counterpart, as only a very small proportion of metallic Pd was detected by XPS (and TEM), with the EXAFS analysis predominantly revealing the presence of the precursor ($[PdCl_4]^{2-}$) species, postreduction.

There are very few reports on the use of NP catalysts for the aerobic oxidation of vanillyl alcohol to vanillin. However, the use of Pt/MOF-5[60] and Pt/C[61] were recently shown to have some activity, but with low TOFs of 4.9 h^{-1} and 19 h^{-1} respectively, in comparison with 93 h^{-1} achieved with our reduced Pt/CuClP material. Other recent studies have explored the use of Co catalysts to catalyze the aerobic oxidation of vanillyl alcohol,[62,63] although the use of a base was mandatory in these systems. In these studies,[62,63] conversion and selectivity toward vanillin appear promising; however, the low substrate to catalyst ratios employed result in inferior TONs at complete conversion. The superior TONs displayed by these extruded catalysts and, in particular, the reduced Pt nanoparticles (Figure 8), which afford TON/TOFs that are at least 4 times higher than existing Pt NP catalysts and almost two-orders of magnitude greater than other transition metal systems (to the best of our knowledge), offers adequate scope for the industrial implementation of these catalysts for the production of vanillin through benign, aerobic oxidation routes.

SUMMARY AND FUTURE PROSPECTS

It has been shown that the $[PtCl_4]^{2-}$ supported porous copper chlorophosphate framework is highly susceptible to complete extrusion by reduction, forming isolated, discrete nanoparticles, which are the loci for aerobic oxidation reactions. The propensity of the Pt NPs to readily extrude from within the porous architecture offers a unique strategy for the design of single-site heterogeneous catalysts, where the nature of the active site can be dexterously manipulated and controlled through judicious activation procedures. The design approach has also facilitated the structural (XRD, EXAFS, TEM) and spectroscopic (XPS, XAS) characterization of the active sites at a molecular level, which have proved invaluable in facilitating structure−property correlations for understanding the implications of the superior activity afforded by reduced Pt particles for the aerobic oxidation of vanillyl alcohol to vanillin.

The study has further established that analogous precursors for generating Au and Pd nanoparticles are sensitive to the thermal activation procedures that are employed, which in turn has a critical influence on the ensuing catalysis. It has been found that reduction procedures under H_2 are more effective than calcinations for extruding the chlorometallate precursors in all three catalysts, but with distinct and varying influences that directly affect the catalytic turnover. While we have identified an efficient route for generating Pt NPs by this route, further studies (currently in progress) will pinpoint activation methodologies that favor complete extrusion of the analogous Au and Pd catalysts.

It is envisaged that this initial investigation will pave the way for further exploring and exploiting the potential of this novel extrusion strategy for generating new nanoparticle catalysts. By using a combination of in situ and operando tools for directly probing the nature of the active site during the activation procedure will afford a greater understanding of how each metal within the framework responds to thermal treatments. This would help establish a detailed understanding of size/shape distributions, compositional integrity, and, more importantly, precise location of the extruded nanoparticles, which could, in turn, facilitate a design-application approach for the controlled engineering of superior catalysts for a wider-range of industrially significant catalytic transformations.

ASSOCIATED CONTENT

Supporting Information

The Supporting Information is available free of charge on the ACS Publications website at DOI: 10.1021/acscatal.5b00481.

Industrial process schemes, EXAFS spectra, XPS data, TEM particle size distribution (PDF)

AUTHOR INFORMATION

Corresponding Author

*E-mail: R.Raja@soton.ac.uk. Tel: (+44)23 8059 2144.

Notes

The authors declare no competing financial interest.

ACKNOWLEDGMENTS

X-ray photoelectron spectra were obtained at the National EPSRC XPS User's Service (NEXUS) at Newcastle University, an EPSRC Mid-Range Facility. We would like to especially thank Dr. Naoko Sano at the NEXUS XPS facility for his help in collecting XPS data and his invaluable advice for data

DOI: 10.1021/acscatal.5b00481
ACS Catal. 2015, 5, 3807−3816

analysis. We thank Diamond Light Source for access to beamline B18 (SP8071-6) that contributed to the results presented here. U.K. Catalysis Hub is kindly thanked for resources and support provided via our membership of the U.K. Catalysis Hub Consortium and funded by EPSRC (portfolio grants EP/K014706/1, EP/K014668/1, EP/K014854/1 and EP/K014714/1). C.S.H. thanks the University of Southampton for a VC scholarship and A*STAR, Singapore for funding under the ARAP award scheme. J.D.H./G.C. acknowledge financial support from Science Foundation Ireland (Grant: 08/CE/I1432) and instrument support from the Electron Microscopy and Analysis Facility (EMAF) at Tyndall.

REFERENCES

(1) Davis, S. E.; Ide, M. S.; Davis, R. J. *Green Chem.* **2013**, *15*, 17−45.
(2) Dimitratos, N.; Lopez-Sanchez, J. A.; Anthonykutty, J. M.; Brett, G.; Carley, A. F.; Tiruvalam, R. C.; Herzing, A. A.; Kiely, C. J.; Knight, D. W.; Hutchings, G. J. *Phys. Chem. Chem. Phys.* **2009**, *11*, 4952−4961.
(3) Enache, D. I.; Edwards, J. K.; Landon, P.; Solsona-Espriu, B.; Carley, A. F.; Herzing, A. A.; Watanabe, M.; Kiely, C. J.; Knight, D. W.; Hutchings, G. J. *Science* **2006**, *311*, 362−365.
(4) Balcha, T.; Strobl, J. R.; Fowler, C.; Dash, P.; Scott, R. W. J. *ACS Catal.* **2011**, *1*, 425−436.
(5) Maclennan, A.; Banerjee, A.; Hu, Y.; Miller, J. T.; Scott, R. W. J. *ACS Catal.* **2013**, *3*, 1411−1419.
(6) Chen, H. W.; Murugadoss, A.; Hor, T. S. A.; Sakurai, H. *Molecules* **2010**, *16*, 149−161.
(7) Hinde, C. S.; Van Aswegen, S.; Collins, G.; Holmes, J. D.; Hor, T. S. A.; Raja, R. *Dalton Trans.* **2013**, *42*, 12600−12605.
(8) Kesavan, L.; Tiruvalam, R.; Rahim, M. H. A.; bin Saiman, M. I.; Enache, D. I.; Jenkins, R. L.; Dimitratos, N.; Lopez-Sanchez, J. A.; Taylor, S. H.; Knight, D. W.; Kiely, C. J.; Hutchings, G. J. *Science* **2011**, *331*, 195−199.
(9) bin Saiman, M. I.; Brett, G. L.; Tiruvalam, R.; Forde, M. M.; Sharples, K.; Thetford, A.; Jenkins, R. L.; Dimitratos, N.; Lopez-Sanchez, J. A.; Murphy, D. M.; Bethell, D.; Willock, D. J.; Taylor, S. H.; Knight, D. W.; Kiely, C. J.; Hutchings, G. J. *Angew. Chem., Int. Ed.* **2012**, *51*, 5981−5985.
(10) Collins, G.; Blömker, M.; Osiak, M.; Holmes, J. D.; Bredol, M.; O'Dwyer, C. *Chem. Mater.* **2013**, *25*, 4312−4320.
(11) Chen, Y.-X.; Lavacchi, A.; Chen, S.-P.; di Benedetto, F.; Bevilacqua, M.; Bianchini, C.; Fornasiero, P.; Innocenti, M.; Marelli, M.; Oberhauser, W.; Sun, S.-G.; Vizza, F. *Angew. Chem., Int. Ed.* **2012**, *51*, 8500−8504.
(12) Cheong, S.; Watt, J. D.; Tilley, R. D. *Nanoscale* **2010**, *2*, 2045−2053.
(13) Henning, A. M.; Watt, J.; Miedziak, P. J.; Cheong, S.; Santonastaso, M.; Song, M.; Takeda, Y.; Kirkland, A. I.; Taylor, S. H.; Tilley, R. D. *Angew. Chem., Int. Ed.* **2013**, *52*, 1477−1480.
(14) Strizhak, P. E. *Theor. Exp. Chem.* **2013**, *49*, 2−21.
(15) Barau, A.; Budarin, V.; Caragheorgheopol, A.; Luque, R.; Macquarrie, D.; Prelle, A.; Teodorescu, V.; Zaharescu, M. *Catal. Lett.* **2008**, *124*, 204−214.
(16) Haruta, M.; Tsubota, S.; Kobayashi, T.; Kageyama, H.; Genet, M. J.; Delmon, B. *J. Catal.* **1993**, *144*, 175−192.
(17) Dimitratos, N.; Villa, A.; Wang, D.; Porta, F.; Su, D.; Prati, L. *J. Catal.* **2006**, *244*, 113−121.
(18) Porta, F.; Prati, L.; Rossi, M.; Scari, G. *J. Catal.* **2002**, *211*, 464−469.
(19) Abad, A.; Corma, A.; García, H. *Chem. - Eur. J.* **2008**, *14*, 212−222.
(20) Raja, R.; Hermans, S.; Shephard, D. S.; Johnson, B. F. G.; Sankar, G.; Bromley, S.; Thomas, J. M. *Chem. Commun.* **1999**, 1571−1572.
(21) Adams, R. D.; Boswell, E. M.; Captain, B.; Hungria, A. B.; Midgley, P. A.; Raja, R.; Thomas, J. M. *Angew. Chem., Int. Ed.* **2007**, *46*, 8182−8185.
(22) Gianotti, E.; Shetti, V. N.; Manzoli, M.; Blaine, J. A. L.; Pearl, W. C.; Adams, R. D.; Coluccia, S.; Raja, R. *Chem. - Eur. J.* **2010**, *16*, 8202−8209.
(23) Raja, R.; Khimyak, T.; Thomas, J. M.; Hermans, S.; Johnson, B. F. G. *Angew. Chem., Int. Ed.* **2001**, *40*, 4638−4642.
(24) Hungria, A. B.; Raja, R.; Adams, R. D.; Captain, B.; Thomas, J. M.; Midgley, P. A.; Golovko, V.; Johnson, B. F. G. *Angew. Chem., Int. Ed.* **2006**, *45*, 4782−4785.
(25) Raja, R.; Adams, R. D.; Blom, D. A.; Pearl, W. C.; Gianotti, E.; Thomas, J. M. *Langmuir* **2009**, *25*, 7200−7204.
(26) Zheng, N.; Stucky, G. D. *J. Am. Chem. Soc.* **2006**, *128*, 14278−14280.
(27) Tasis, D.; Tagmatarchis, N.; Bianco, A.; Prato, M. *Chem. Rev.* **2006**, *106*, 1105−1136.
(28) Laursen, A. B.; Højholt, K. T.; Lundegaard, L. F.; Simonsen, S. B.; Helveg, S.; Schüth, F.; Paul, M.; Grunwaldt, J.-D.; Kegnæs, S.; Christensen, C. H.; Egeblad, K. *Angew. Chem., Int. Ed.* **2010**, *49*, 3504−3507.
(29) Zhang, X.; Ke, X.; Zhu, H. *Chem. - Eur. J.* **2012**, *18*, 8048−8056.
(30) Lu, G.; Li, S.; Guo, Z.; Farha, O. K.; Hauser, B. G.; Qi, X.; Wang, Y.; Wang, X.; Han, S.; Liu, X.; DuChene, J. S.; Zhang, H.; Zhang, Q.; Chen, X.; Ma, J.; Loo, S. C. J.; Wei, W. D.; Yang, Y.; Hupp, J. T.; Huo, F. *Nat. Chem.* **2012**, *4*, 310−316.
(31) Esken, D.; Turner, S.; Lebedev, O. I.; Van Tendeloo, G.; Fischer, R. A. *Chem. Mater.* **2010**, *22*, 6393−6401.
(32) White, R. J.; Luque, R.; Budarin, V. L.; Clark, J. H.; Macquarrie, D. J. *Chem. Soc. Rev.* **2009**, *38*, 481−494.
(33) Cheetham, A. K.; Férey, G.; Loiseau, T. *Angew. Chem., Int. Ed.* **1999**, *38*, 3268−3292.
(34) Leithall, R. M.; Shetti, V. N.; Maurelli, S.; Chiesa, M.; Gianotti, E.; Raja, R. *J. Am. Chem. Soc.* **2013**, *135*, 2915−2918.
(35) Thomas, J. M.; Raja, R. *Chem. Commun.* **2001**, 675−687.
(36) Thomas, J. M. *Proc. R. Soc. London, Ser. A* **2012**, *468*, 1884−1903.
(37) Huang, Q.; Ulutagay, M.; Michener, P. A.; Hwu, S.-J. *J. Am. Chem. Soc.* **1999**, *121*, 10323−10326.
(38) Williams, E. R.; Leithall, R. M.; Raja, R.; Weller, M. T. *Chem. Commun.* **2013**, *49*, 249−251.
(39) Fahlbusch, K.-G.; Hammerschmidt, F.-J.; Panten, J.; Pickenhagen, W.; Schatkowski, D.; Bauer, K.; Garbe, D.; Surburg, H. Flavors and Fragrances. *Ullmann's Encyclopedia of Industrial Chemistry*, 7th ed.; Wiley-VCH Verlag GmbH & Co. KGaA: Weinheim, 2003; Vol. *15*, pp 73−198.
(40) Vidal, J.-P. Vanillin. *Kirk-Othmer Encyclopedia of Chemical Technology*; John Wiley & Sons, Inc.: New York, 2006; pp 1−14.
(41) Metivier, P. Method for preparing a 4-hydroxybenzaldehyde and derivatives. U.S. Patent No. 6,184,421 B1, February 6, 2001.
(42) Hansen, J.; Hansen, E. H.; Sompalli, H. P.; Sheridan, J. M.; Heal, J. R.; Hamilton, W. D. O. Compositions and methods for the biosynthesis of vanillin or vanillin beta-d-glucoside. Patent No. WO 2013022881 A1, April 3, 2013.
(43) Frost, J. W. Synthesis of vanillin from a carbon source. U.S. Patent No.US 6372461 B1, 2002.
(44) Zope, B. N.; Hibbitts, D. D.; Neurock, M.; Davis, R. J. *Science* **2010**, *330*, 74−78.
(45) Sheldon, R. A. *Chem. Soc. Rev.* **2012**, *41*, 1437−1451.
(46) Arends, I. W. C. E.; Sheldon, R. A.; Backvall, J.-E. Modern Oxidation of Alcohols Using Environmentally Benign Oxidants. In *Modern Oxidation Methods*; Backvall, J.-E., Ed.; Wiley-VCH: Weinheim, 2005; pp 83−118.
(47) Fairley, N.; Carrick, A. *The Casa Cookbook*; Acolyte science: Cheshire, U.K., 2005; pp 1−368.
(48) Newville, M. *J. Synchrotron Radiat.* **2001**, *8*, 322−324.
(49) Ravel, B.; Newville, M. *J. Synchrotron Radiat.* **2005**, *12*, 537−541.
(50) Beale, A. M.; Weckhuysen, B. M. *Phys. Chem. Chem. Phys.* **2010**, *12*, 5562−5574.

DOI: 10.1021/acscatal.5b00481
ACS Catal. 2015, 5, 3807−3816

(51) *Catalysis by Gold*; Bond, G. C.; Louis, C.; Thompson, D. T., Eds.; Catalytic Science Series; Hutchings, G. J., Series Ed; Imperial College Press: London, UK, 2006; Vol. *6*, pp 1−383.
(52) Miller, J. T.; Kropf, A. J.; Zha, Y.; Regalbuto, J. R.; Delannoy, L.; Louis, C.; Bus, E.; van Bokhoven, J. A. *J. Catal.* **2006**, *240*, 222−234.
(53) Turner, M.; Golovko, V. B.; Vaughan, O. P. H.; Abdulkin, P.; Berenguer-Murcia, A.; Tikhov, M. S.; Johnson, B. F. G.; Lambert, R. M. *Nature* **2008**, *454*, 981−983.
(54) Li, C.; Wang, Y.; Guo, X.; Jiang, Z.; Jiang, F.; Zhang, W.; Zhang, W.; Fu, H.; Xu, H.; Wu, G. *J. Phys. Chem. C* **2014**, *118*, 3140−3144.
(55) Tan, Y. W.; Dai, X. H.; Li, Y. F.; Zhu, D. B. *J. Mater. Chem.* **2003**, *13*, 1069−1075.
(56) Diaz, C.; Valenzuela, M. L.; Bravo, D.; Dickinson, C.; O'Dwyer, C. *J. Colloid Interface Sci.* **2011**, *362*, 21−32.
(57) Ng, Y. H.; Ikeda, S.; Morita, Y.; Harada, T.; Ikeue, K.; Matsumura, M. *J. Phys. Chem. C* **2009**, *113*, 12799−12805.
(58) Wang, X.; Andrews, L. *Angew. Chem., Int. Ed.* **2003**, *42*, 5201−5206.
(59) Ramu, R.; Ravindra Nath, N.; Reddy, M. R.; Das, B. *Synth. Commun.* **2004**, *34*, 3135−3145.
(60) Tarasov, A. L.; Kustov, L. M.; Isaeva, V. I.; Kalenchuk, A. N.; Mishin, I. V.; Kapustin, G. I.; Bogdan, V. I. *Kinet. Catal.* **2011**, *52*, 273−276.
(61) Tarasov, A. L.; Kustov, L. M.; Bogolyubov, A. A.; Kiselyov, A. S.; Semenov, V. V. *Appl. Catal., A* **2009**, *366*, 227−231.
(62) Zakzeski, J.; Dębczak, A.; Bruijnincx, P. C. A.; Weckhuysen, B. M. *Appl. Catal., A* **2011**, *394*, 79−85.
(63) Garade, A. C.; Biradar, N. S.; Joshi, S. M.; Kshirsagar, V. S.; Jha, R. K.; Rode, C. V. *Appl. Clay Sci.* **2011**, *53*, 157−163.

DOI: 10.1021/acscatal.5b00481
ACS Catal. 2015, 5, 3807−3816